

# Rational Core–Shell Design of Open Air Low Temperature In Situ Processable CsPbI<sub>3</sub> Quasi-Nanocrystals for Stabilized p-i-n Solar Cells

Jun Xi, Chengcheng Piao, Junseop Byeon, Jungjin Yoon, Zhaoxin Wu,\* and Mansoo Choi\*

As a promising alternative, inorganic perovskite nanocrystals allow reinforced stability of photovoltaic device. Unfortunately, directly assembling these nanocrystals into film is uncontrollable. Instead, in situ assembling technology under low temperature in open air is attractive but limited due to the tendency of nonperovskite transition. The adverse shell ligands and unstable core lattices are known as the fundamental problems. In order to address this issue, here proposed is a rational core–shell design: 1) with respect to ligands, a new one, 4-fluorophenethylammonium iodide, is used to enhance bonding force and charge coupling between ligands and nanocrystals; 2) with respect to lattices, a novel compound H<sub>2</sub>PbI<sub>4</sub> is employed to assist divalent ion (Mn<sup>2+</sup>) doping into perovskite lattices. By low temperature in situ processing CsPbI<sub>3</sub> quasi-nanocrystal film, the highest power conversion efficiency of 13.4% for p-i-n solar cells is achieved, which retains 92% after 500 h in ambient air. The current study underlines the significance of rational hierarchical design of inorganic perovskite nanocrystals, especially for low temperature in situ processable electronic devices.

## 1. Introduction

Hybrid organic–inorganic perovskites demonstrate great potential in photovoltaic fields owing to their excellent semiconductor properties.<sup>[1–5]</sup> However, the instability of perovskites-based device still hinders their entry to commercial market.<sup>[6]</sup> Considering the chemical compositions, the volatile organic moieties (such as methylammonium, formamidinium) can easily react with oxygen and water to form superoxides and hydrates, thus dismantling perovskite octahedral units.<sup>[7–9]</sup> As a result, the devices are prone to degrade.

Instead of organic moieties, inorganic moieties could endow perovskites with better stability against ambient environment.<sup>[10]</sup> In this scenario, inorganic cesium perovskites (CsPbX<sub>3</sub>, X is a halide anion) with suitable tolerance factor  $t$  ( $0.8 < t < 1.0$ ) have been developed.<sup>[11]</sup>

Aiming at photovoltaic fields, CsPbI<sub>3</sub> with suitable bandgap (1.73 eV) is viewed as a promising candidate.<sup>[12]</sup> Unfortunately, this material shows different energy disorders and crystal phases, impeding stabilization of devices. The black  $\alpha$  phase ( $Pm3m$ ) of CsPbI<sub>3</sub> should be obtained by heating the yellow  $\delta$  phase ( $Pnma$ ) above 585 K.<sup>[13]</sup> However, this high temperature will limit potential application of CsPbI<sub>3</sub>. Currently, low temperature ( $\leq 100$  °C) processable p-i-n solar cells are becoming more attractive because the structures can render them compatible with roll-to-roll deposition on flexible substrates.<sup>[14–17]</sup> Thus, depositing stabilized CsPbI<sub>3</sub> film under low temperature is imperative toward p-i-n solar cells. Researchers have proposed different methods to solve this problem, such as polymer templated,<sup>[18]</sup> adducts controlled,<sup>[19–22]</sup> ions doped,<sup>[23]</sup> crystal regulated,<sup>[24]</sup> and nanocrystals presynthesized methods.<sup>[25–28]</sup> Most recently, over 17% efficiency is reported based on multifunctional ions management for n-i-p structure.<sup>[29]</sup> Aside from these, CsPbI<sub>3</sub> crystal lattices in nanocrystal colloidal solutions feature more stabilized cubic structure due to strong quantum confinement effect and high surface Gibbs energy from the contribution of large surface/volume ratio.<sup>[24]</sup> To further stabilize metastable perovskite phase of CsPbI<sub>3</sub> nanocrystals, doping with divalent ions has been suggested on account of the contracted lattice with excess configurational entropy.<sup>[30–32]</sup>

Nevertheless, the complicated presynthesis and purification processes hinder directly assembling nanocrystals into film.

Dr. J. Xi, C. Piao, J. Byeon, Dr. J. Yoon, Prof. M. Choi  
Global Frontier Center for Multiscale Energy Systems  
Seoul National University  
Seoul 08826, Republic of Korea  
E-mail: mchoi@snu.ac.kr

C. Piao, J. Byeon, Prof. M. Choi  
Department of Mechanical and Aerospace Engineering  
Seoul National University  
Seoul 08826, Republic of Korea

Dr. J. Yoon  
Photo-Electronic Hybrids Research Center  
National Agenda Research Division  
Korea Institute of Science and Technology  
Seoul 02792, Republic of Korea

Prof. Z. Wu  
Key Laboratory for Physical Electronics and Devices of the Ministry  
of Education & Shaanxi Key Lab of Information Photonic Technique  
School of Electronic and Information Engineering  
Xi'an Jiaotong University  
No. 28, Xianning West Road, Xi'an 710049, China  
E-mail: zhaoxinwu@mail.xjtu.edu.cn

Prof. Z. Wu  
Collaborative Innovation Center of Extreme Optics  
Shanxi University  
Taiyuan 030006, China

The ORCID identification number(s) for the author(s) of this article can be found under <https://doi.org/10.1002/aenm.201901787>.

DOI: 10.1002/aenm.201901787

Besides, undesirable ligands and unstable lattices hinder the device application of nanocrystals. Hence, a design of open air low temperature in situ processable CsPbI<sub>3</sub> nanocrystals is urgently required for p-i-n solar cells.<sup>[19,25]</sup> Herein, a rational core (lattice)–shell (ligand) structure is regarded as the key issue of in situ nanocrystal fabrication. With respect to the ligand, the following problems should be of awareness: 1) during the purification of nanocrystals, traditional oleylammonium/octylamine (OA) ligands can be easily washed off on account of weak acid–base interaction between [PbI<sub>6</sub>]<sup>4−</sup> units and ligands.<sup>[33,34]</sup> As a result, massive nanocrystals are apt to aggregate, thus inducing irreversible phase transition (Figure 1a).<sup>[35]</sup> 2) Alkyl ligands (such as OA) would undermine charge coupling between nanocrystals, which leads to deficient charge extraction in devices (Figure 1a).<sup>[33]</sup> With respect to the lattice, the crucial problem is that under high M/Pb ratio (where M is doping divalent ion), PbI<sub>2</sub> easily precipitates. This phenomenon can be attributed to the small driving force, which makes doping self-limited and unavailable (Figure 1b).<sup>[30]</sup>

To address aforementioned problems, an approach is proposed for open air low temperature in situ processable CsPbI<sub>3</sub> quasi-nanocrystals (QNCs) (QNCs denote the stabilized nanocrystals of size larger than Bohr diameter (12 nm) with high surface Gibbs energy instead of strong quantum confinement effect): 1) with regard to the ligand, we used a bifunctional ligand, 4-fluorophenethylammonium iodide (FPEAI). This ligand has a conjugated aromatic ammonium group terminated with strong electronegative fluoride. Its highly polarized structure can enhance bonding force between ligand and CsPbI<sub>3</sub> lattice, thus precluding ligand stripped, preserving crystal size, and reinforcing lattice. In addition, the conjugated groups can warrant efficient charge coupling between nanocrystals, which can efficiently enhance charge extraction in the device (Figure 1a). 2) With regard to the lattice, we synthesize a novel compound, H<sub>2</sub>PbI<sub>4</sub>, which was obtained from PbI<sub>2</sub> coordinated with two hydrogen iodide (HI) molecules. This material can increase the solubility of doped divalent ions (Mn<sup>2+</sup>) in precursors, which assists Mn<sup>2+</sup> doping into host lattice instead

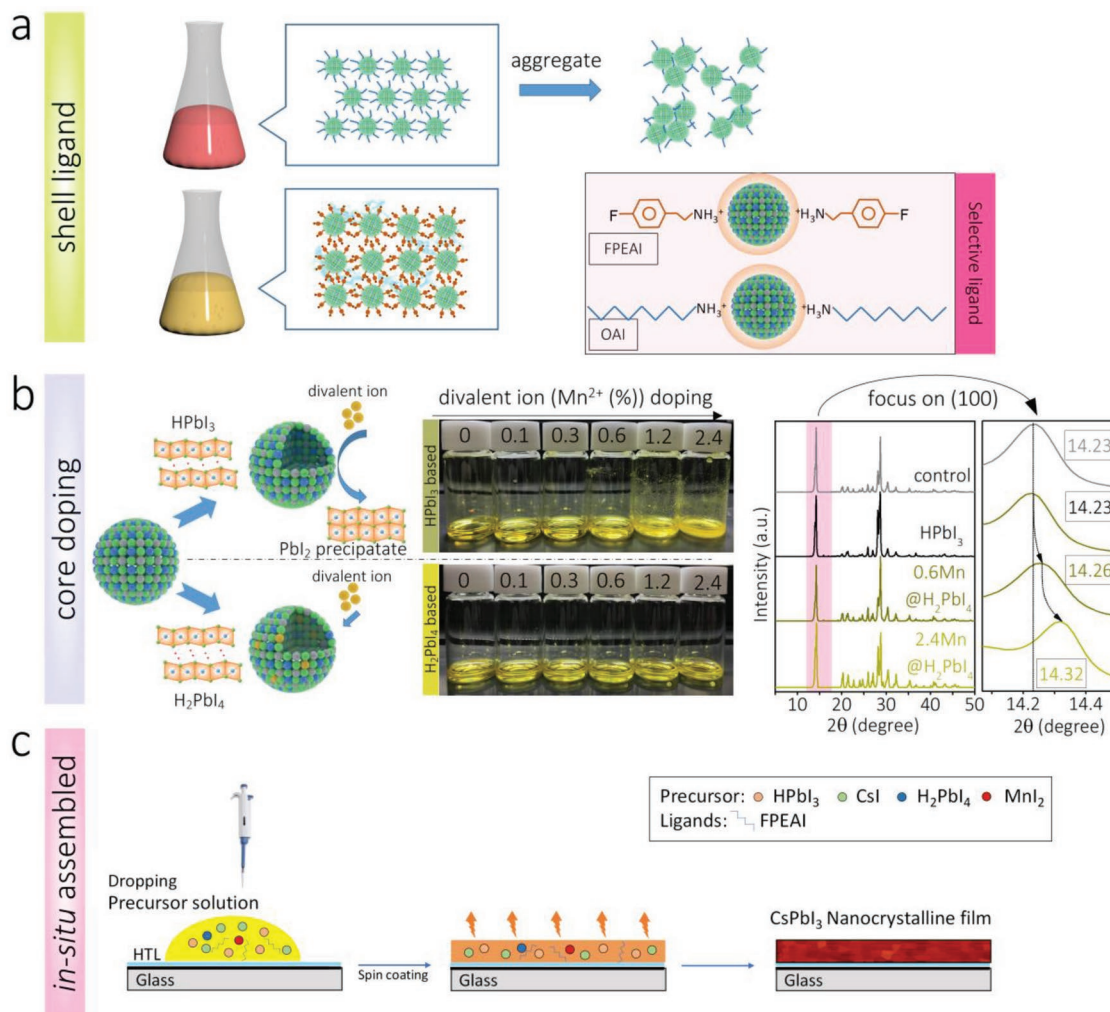


**Figure 1.** Schematic: a) Bonding interactions between nanocrystals confined by OAI and FPEAI ligands. b) Divalent ions (Mn<sup>2+</sup>) doping process based on HPbI<sub>3</sub> and based on excess addition of H<sub>2</sub>PbI<sub>4</sub>, XRD patterns of inset show control sample, HPbI<sub>3</sub>-based sample, 0.6% and 2.4% Mn<sup>2+</sup>-doped sample with an addition of equal amount of H<sub>2</sub>PbI<sub>4</sub>. c) Procedure of in situ assembled CsPbI<sub>3</sub> QNC films.

of interstitial vacancy (X-ray diffraction (XRD) in Figure 1b). Based on such rational design, we successfully in situ assembled  $\text{CsPbI}_3$  QNC films into p-i-n solar cell under low temperature in open air (Figure 1c). As a result, a highest power conversion efficiency (PCE) of 13.4% was achieved, maintaining 92% after 500 h stored in ambient air. The present study suggests a guideline for rational design of in situ processable perovskite nanocrystals, paving the way particularly for robust nanocrystal electronic devices, such as solar cells, light-emitting diodes, photodetectors, and related flexible devices.

## 2. Results and Discussions

The powders of all the key materials are shown in Figure 2a. The detailed synthesis procedures are described in the Experimental Section. Briefly, OAI and FPEAI were obtained by reacting OA and FPEA with excess HI solutions, respectively. Then the products were purified and confirmed by NMR spectrum (Figure S1, Supporting Information). In addition,  $\text{HPbI}_3$  and  $\text{H}_2\text{PbI}_4$  were synthesized by reacting 1 mol  $\text{PbI}_2$  with 1.5 mol and 2.5 mol HI solutions, respectively. Afterward, the

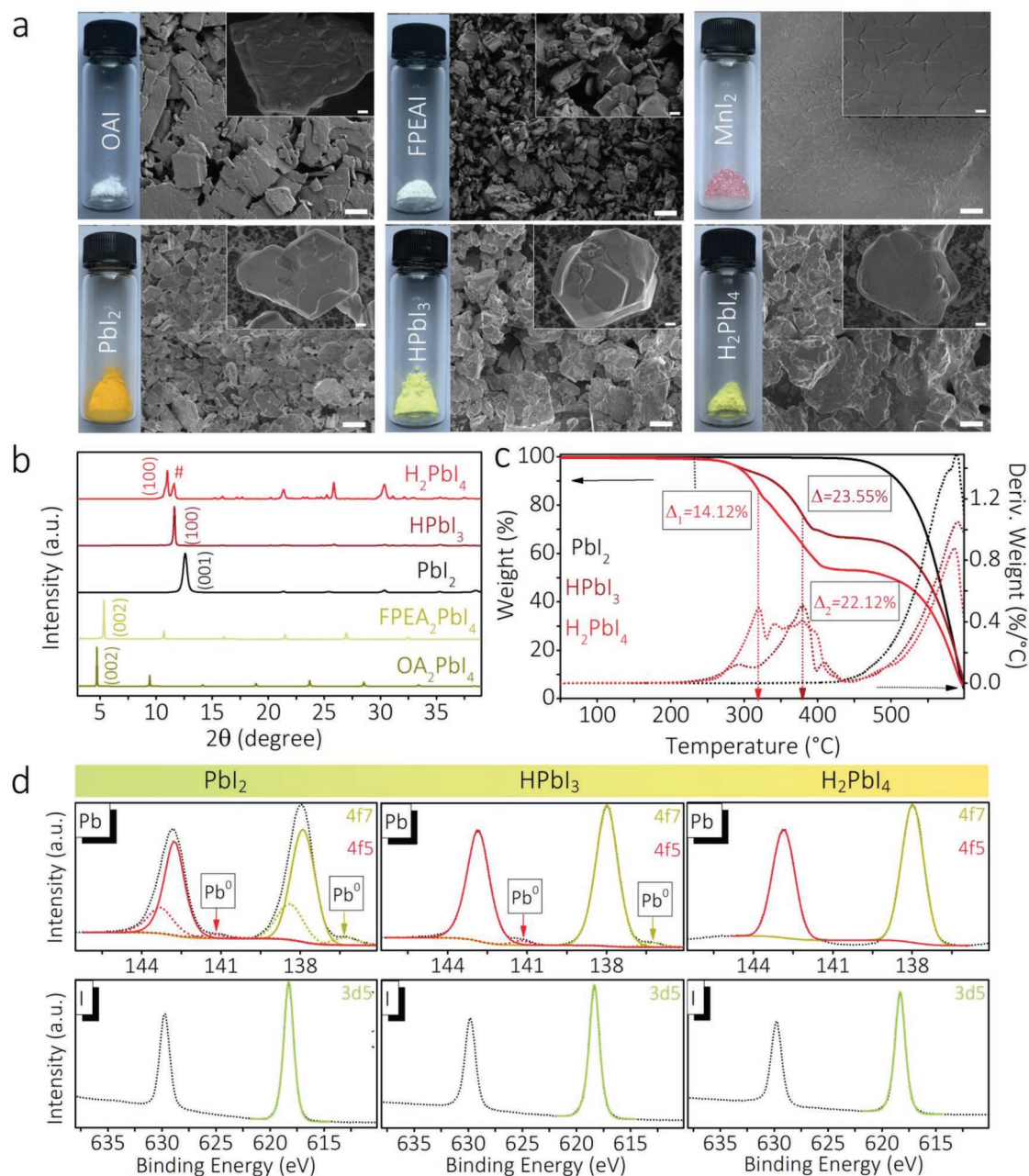


**Figure 2.** a) SEM images of different material powders used in this work, scale bar: 2  $\mu\text{m}$  in high magnification and 20  $\mu\text{m}$  in low magnification (inset images), respectively. b) XRD patterns of corresponding material powders. c) TGA and d) XPS spectra of  $\text{PbI}_2$ ,  $\text{HPbI}_3$ , and  $\text{H}_2\text{PbI}_4$  powders.



products were obtained by washing with diethyl ether. All the powders above are washed and dried in the same manner.

The morphology of each material is shown as scanning electron microscopy (SEM) image in Figure 2a. In terms of ligand materials, both of OAI and FPEAI crystals are uniformly distributed. Due to longer alky chains of OAI molecules, the mean size of OAI crystal is around ten times larger than that of FPEAI crystal. In terms of lead compound materials, hexagonal HPbI<sub>3</sub> crystals are thicker than PbI<sub>2</sub>, which results from PbI<sub>2</sub> lattice expanding along (001) plane.<sup>[36,37]</sup> Similarly, H<sub>2</sub>PbI<sub>4</sub> crystals have larger thickness than HPbI<sub>3</sub> due to further expanded (100) plane of HPbI<sub>3</sub>. In addition, the divalent dopant MnI<sub>2</sub> shows high quality of sheet crystals. In order to understand the differences of above crystals, high-resolution XRD was employed (Figure 2b). Here, instead of ligand materials, monolayer 2D Ruddlesden–Popper perovskites formed by reacting ligands/PbI<sub>2</sub> (1/1) were measured due to their highly recognizable orthorhombic lattices. We can find that (002) planes of OA<sub>2</sub>PbI<sub>4</sub> and FPEAI<sub>2</sub>PbI<sub>4</sub> are located at 4.72° and 5.35°, respectively, indicating around 18.7 and 16.5 Å of the plane distance. These values agree well with the respective molecular chains of above two ligands. As for the lead compounds, PbI<sub>2</sub> has orthorhombic space groups featuring (001) plane at 12.6°, and HPbI<sub>3</sub> possesses similar space groups featuring (100) plane at 11.6°. This difference reveals that HPbI<sub>3</sub> is formed from PbI<sub>2</sub> lattice introduced by 1 mol HI, where the original plane distance (7.02 Å) increases to 7.60 Å.<sup>[36]</sup> H<sub>2</sub>PbI<sub>4</sub> shows the dominant peak at 11.0°, which belongs to (100) plane of H<sub>2</sub>PbI<sub>4</sub> (the fitting details are given in Figure S2, Supporting Information). Besides, another minor peak at 11.6° represents a little mixed HPbI<sub>3</sub>. We deduced that H<sub>2</sub>PbI<sub>4</sub> is formed from HPbI<sub>3</sub> lattice combined with 1 mol HI, where the plane distance (7.60 Å) increases to 8.02 Å. Besides, the XRD patterns (Figure S2, Supporting Information) of high-quality H<sub>2</sub>PbI<sub>4</sub> crystals made by antisolvent diffusion method have same diffraction features, proving the enlarged (100) plane compared to HPbI<sub>3</sub>. The optimized lattice parameters of H<sub>2</sub>PbI<sub>4</sub> and HPbI<sub>3</sub> are summarized in Table S1 in the Supporting Information.

We used thermogravimetric (TGA; Figure 2c) in N<sub>2</sub> to further analyze the chemical compositions of these compounds. As the reference, PbI<sub>2</sub> is found to start to decompose at around 400 °C. HPbI<sub>3</sub> lost weight at two points around 240 and 400 °C, indicating the starting decomposition of HI and PbI<sub>2</sub>, respectively. Similarly, H<sub>2</sub>PbI<sub>4</sub> involves two decomposition stages. However, we realize a little differences of the weight loss rate: 1) for HPbI<sub>3</sub>, around 23.55% weight ( $\Delta$ ) is lost at 379.5 °C at the highest rate of 0.5% °C<sup>-1</sup>, implying that HI bonding is completely broken. Accordingly, we deduce that the molar ratio between HI and PbI<sub>2</sub> should be around 1.08:1. 2) For H<sub>2</sub>PbI<sub>4</sub>, about 14.12% weight ( $\Delta_1$ ) is first lost at 320.2 °C at the highest rate of 0.49% °C<sup>-1</sup>, and then 22.12% weight ( $\Delta_2$ ) is lost at 379.8 °C at the second highest rate of 0.41% °C<sup>-1</sup>. This result reveals that the decomposition process of HI bonding should be considered as two stages, and the molar ratio between HI and PbI<sub>2</sub> is almost 1.97:1. During the decomposition, this first stage is induced by breaking weaker HI bonding from sublattice, and the second stage is a result of other HI releases from residual H<sub>2</sub>PbI<sub>4</sub>. To learn more about the compositions, we examined X-ray photoelectron spectra (XPS) (shown in Figure 2d and

Figure S3, Supporting Information). By integrating the area of each element, the ratio of I/Pb in PbI<sub>2</sub>, HPbI<sub>3</sub>, and H<sub>2</sub>PbI<sub>4</sub> was estimated to about 1.96, 3.11, and 4.03, confirming their expected chemical formula. What is more, different from obvious metallic Pb<sup>0</sup> traces of PbI<sub>2</sub> and HPbI<sub>3</sub>, H<sub>2</sub>PbI<sub>4</sub> does not contain these oxidized traces, suggesting its fully bonding of 4f orbitals. Intriguingly, the compositions of the two kinds of HI-coordinated compounds are similar to those of the reported dimethyl sulfoxide (DMSO)-coordinated compounds PbI<sub>2</sub>(DMSO) and PbI<sub>2</sub>(DMSO)<sub>2</sub>.<sup>[38]</sup> Hence, we can regard them as PbI<sub>2</sub>(HI) and PbI<sub>2</sub>(HI)<sub>2</sub>, respectively. In addition, the properties of solution processed films of above-mentioned materials can be found in Figure S4 in the Supporting Information. We find similar wide bandgap of OA<sub>2</sub>PbI<sub>4</sub> and FPEAI<sub>2</sub>PbI<sub>4</sub> from photoluminescence (PL) and UV-vis absorption (Abs) spectra, implying quantum confined effect between OAI/FPEAI ligands and [PbI<sub>6</sub>]<sup>4-</sup> units. Besides, compared to HPbI<sub>3</sub> film, H<sub>2</sub>PbI<sub>4</sub> film shows much more pinholes. Generally, HI can be easily evaporated during annealing. Hence, plenty of pinholes in H<sub>2</sub>PbI<sub>4</sub> film are well matched with the excessive HI contents in its molecule.

Since above ligands are used in CsPbI<sub>3</sub> nanocrystals, it is necessary to evaluate the bonding force and charge coupling between CsPbI<sub>3</sub> lattices and OAI/FPEAI ligands. Here, we employed TGA and space charge limited current analysis to estimate the thermostability and conductivity of OAI/FPEAI confined CsPbI<sub>3</sub> sublattices, (OA)<sub>2</sub>CsPb<sub>2</sub>I<sub>7</sub> and (FPEA)<sub>2</sub>CsPb<sub>2</sub>I<sub>7</sub>, respectively (Figures S5 and S6, Supporting Information). It can be observed that (FPEA)<sub>2</sub>CsPb<sub>2</sub>I<sub>7</sub> possesses a decomposition temperature of 277 °C, around 10 °C higher than (OA)<sub>2</sub>CsPb<sub>2</sub>I<sub>7</sub>. This difference is probably caused by higher polarization from strong electronegative fluoride. Moreover, the conductivity of (FPEA)<sub>2</sub>CsPb<sub>2</sub>I<sub>7</sub> film is two orders of magnitude higher than that of (OA)<sub>2</sub>CsPb<sub>2</sub>I<sub>7</sub> film owing to the short conjugated aromatic group of FPEAI. These results confirm that lattice stability and charge transfer between CsPbI<sub>3</sub> lattices and FPEAI ligands are significantly enhanced.

After assessing the fundamentals of the designed materials, we in situ assembled CsPbI<sub>3</sub> QNC films for low temperature processable p-i-n device. All the CsPbI<sub>3</sub> films were deposited on Glass/ITO (indium tin oxide)/PTAA (poly[bis(4-phenyl)(2,4,6-trimethylphenyl)amine] substrates in open air. We found that the as-spun films in open air were already composed of nanocrystals. By comparison, the as-spun films in glovebox were amorphous, and started to crystallize after annealing in 10 s (Figure S7, Supporting Information). Besides, the crystals made in open air are more uniform and smaller compared to those in glovebox. According to such differences, we deduce the formation mechanism of in situ nanocrystals as follows: Perovskite solutions are composed of lead polyhalide colloids, which act as building block for crystals. In open air, there is a proton transfer process caused by H<sub>2</sub>O molecules: DMF · xHI + xH<sub>2</sub>O = DMF + H<sub>3</sub>O<sup>+</sup> + xI<sup>-</sup>.<sup>[39]</sup> The solvent/proton acidity or I<sup>-</sup> concentration is reported to reduce the colloid size. During spin-coating process in ambient air, I<sup>-</sup> coordinated with reduced PbI<sub>2</sub> colloids assisted by H<sub>2</sub>O and ligand FPEAI together quickly form [PbI<sub>6</sub>]<sup>4-</sup> units interacted Cs<sup>+</sup>. In this case, high-quality nanocrystals can be simultaneously formed during spinning.

The optimization of materials and solvents of precursors are shown in Figures S8 and S9 in the Supporting Information. Here  $\text{Mn}^{2+}$  was selected as dopant owing to its high formation energy. In parallel,  $\text{Mn}^{2+}$  doping can prevent formation of other nonperovskites.<sup>[32]</sup> During the optimized process, we realized that  $\text{MnI}_2$  has limited solubility in precursors (Figure 1b). To intrinsically assist  $\text{Mn}^{2+}$  doping, equal molar  $\text{H}_2\text{PbI}_4$  versus  $\text{Mn}^{2+}$  was used to replace fractions of  $\text{HPbI}_3$  in precursors. XRD patterns in Figure 1b demonstrate that (100) planes obviously shift toward higher degree upon 0.6–2.4%  $\text{Mn}^{2+}$  doping with addition of  $\text{H}_2\text{PbI}_4$ , indicating the crystal lattice is contracted. Such contraction phenomenon is induced by shortening Pb-I bonds, proving that  $\text{Mn}^{2+}$  is intrinsically doped into lattices.<sup>[31,32]</sup> The word “assist” here is mainly used to describe the phenomenon that the addition of  $\text{H}_2\text{PbI}_4$  can significantly increase the concentrations of  $\text{Mn}^{2+}$  and avoid  $\text{PbI}_2$  precipitations, resulting in more efficient doping of  $\text{Mn}^{2+}$  into perovskite lattices. This trend may be caused by that more iodide ions from  $\text{H}_2\text{PbI}_4$  can be coordinated with  $\text{Pb}^{2+}$  ions based on a soft acid–base principle, thus reducing the radius of the lead-solvent colloid clusters to avoid  $\text{PbI}_2$  precipitations. It can be found that the best QNC film is formed from stoichiometric ratios of  $\text{HPbI}_3$ , CsI and excess FPEAI,  $\text{H}_2\text{PbI}_4$ ,  $\text{MnI}_2$ . Morphologies of  $\text{CsPbI}_3$  QNC films fabricated using different ratios of FPEAI and  $\text{Mn}^{2+}$  can be observed in Figure S9 in the Supporting Information. The best quality QNC films were obtained based on 5.0% FPEAI and 0.6%  $\text{Mn}^{2+}$  doping. Recently, some works suggest that  $\text{HPbI}_3$  will induce dimethylammonium (DMA) ions doping into inorganic perovskites.<sup>[40]</sup> However, our samples do not share the same NMR peaks of DMA (Figure S10, Supporting Information), implying absence of DMA in the final QNC films. There may be traces of DMA and further study is encouraged on this DMA hybrid crystals. Besides, UV-vis Abs and steady-state PL spectra of all the films are exhibited in Figures S11 and S12 in the Supporting Information. We observe that the films with higher FPEAI (>5%) exhibit a new PL peak of around 570 nm, which is ascribed to the emerged 2D perovskites with higher energy excitons. The XRD patterns in Figure S13 in the Supporting Information also agree well with morphologies of these QNC films. Based on these observations, we derive the optimized ratios of FPEAI and  $\text{H}_2\text{PbI}_4$  of 5.0% and 0.6%, respectively.

To deeply study our low temperature in situ processable  $\text{CsPbI}_3$  QNC films, four kinds of samples were fabricated: 1) without ligands, 2) with OAI ligands, 3) with FPEAI ligands, 4) with co-addition of FPEAI and  $\text{Mn}^{2+}$ . We have summarized the properties of above films in **Figure 3**. As shown in SEM images in Figure 3a (statistical distribution of crystal size of different samples can be found in Figure S14, Supporting Information), it can be concluded as follows: First, the controlled sample is composed of hundred nanometer-sized crystals due to lack of ligand confinement. In the meanwhile, obvious pin-holes are formed. Second, OAI ligands-based film shows nonuniform topography with smaller sized crystals. This character is probably resulted from stripping of partial OAI ligands with weaker bonding force.<sup>[41]</sup> Third, FPEAI ligands-based sample is composed of around 30 nm crystals, and the film becomes much more homogenous. The main reason we considered is the strengthened bonding force between FPEAI ligands and

perovskite lattice. Last, the quality of the synergistic film with FPEAI ligands and  $\text{Mn}^{2+}$  doping surpasses that of other three films, revealing the significance of rational design of ligands and lattices. Irrespective of the film quality, XRD patterns in Figure 3b demonstrate high qualities of  $\alpha$  phases without  $\delta$  phases in any sample. We can estimate the crystal size from Debye–Scherrer equation, given by  $D_{\text{size}} = K\lambda/B_{\text{size}}\cos\theta$ , where  $D_{\text{size}}$  is Scherrer crystallite size,  $K$  is a unit cell geometry-dependent constant,  $\lambda$  is the X-ray wavelength ( $\lambda = 1.5418 \text{ \AA}$ ),  $B_{\text{size}}$  is the peak width broadening due to the size effect, and  $\theta$  is the Bragg angle. The fitting results are shown in Figure S15 in the Supporting Information, where a similar variation trend of crystal size was compared to that of SEM images. Importantly, different from other films, QNC film with co-addition of FPEAI and  $\text{Mn}^{2+}$  shows (100) plane at  $14.26^\circ$  instead of  $14.23^\circ$  (Figure S16, Supporting Information), implying the crystal lattice is contracted due to  $\text{Mn}^{2+}$  doping.<sup>[30]</sup> A little (002) plane at lower degree splitting from (100) plane may originate from slightly distorted  $[\text{PbI}_6]^{4-}$  units. Abs spectra in Figure 3c show the QNC film with co-addition of FPEAI and  $\text{Mn}^{2+}$  has the highest intensity of light absorption. Similarly, this QNC film possesses the highest PL intensity (Figure 3d), indicating that the exciton radiative recombination is significantly increased. On account of the larger crystal sizes of all the samples compared to the Bohr diameter (12 nm) of  $\text{CsPbI}_3$ , the unconfined or weakly quantum confined excitons could induce similar bandgap and PL peaks similar to bulk materials.<sup>[42]</sup> Notably, there is a little blue-shift of PL peak after introducing FPEAI and  $\text{Mn}^{2+}$  together, which might originate from the following reasons: In terms of ligands, coulomb force between charges in the mutual crystal lattices can increase due to the generation of electric field by charge extending into ligands.<sup>[43]</sup> FPEAI with a higher dielectric constant than OAI will decrease such coulomb force between charges in the nanocrystals, thereby increasing the coulomb screening effect. In this case, a more efficient radiative band-to-band recombinations with an increased defect tolerance will be achieved, thus inducing a blue-shifted PL peak.<sup>[44]</sup> In terms of lattices, Mn doping will enable the lattice contraction to slightly increase the bandgap, thus generating a more blue-shifted PL peak.<sup>[32]</sup> Encouragingly, time-resolved PL (TRPL) spectra (Figure 3e) demonstrates that the carrier lifetime progressively increases from 38 ns (in the controlled film) to 48 ns (in the QNC film), revealing superior carrier transport. Such improvement can be attributed to efficient charge transfer between mutual lattices assisted by the conjugated ligands and suppressed defects from  $\text{Mn}^{2+}$  doping. It is worth noting that the optimized  $\text{CsPbI}_3$  QNC film shows the best stability in ambient air (Figure 3f) (the details of PL change dependent on ratios of ligands and dopants can be found in Figures S17 and S18, Supporting Information). Besides, XRD patterns (Figure 3g) and Abs spectra (Figure S19, Supporting Information) of the degraded samples confirm the improved stability. The enhanced bonding force between FPEAI ligands and  $\text{CsPbI}_3$  lattices, the conjugated aromatic rings in FPEAI molecules, and the reduced traps from  $\text{Mn}^{2+}$  doping should be comprehensive reasons accounting for all improvements. In summary, this rational designed low temperature in situ processable  $\text{CsPbI}_3$  QNC film demonstrates much improved both optoelectronic properties and environmental stability.

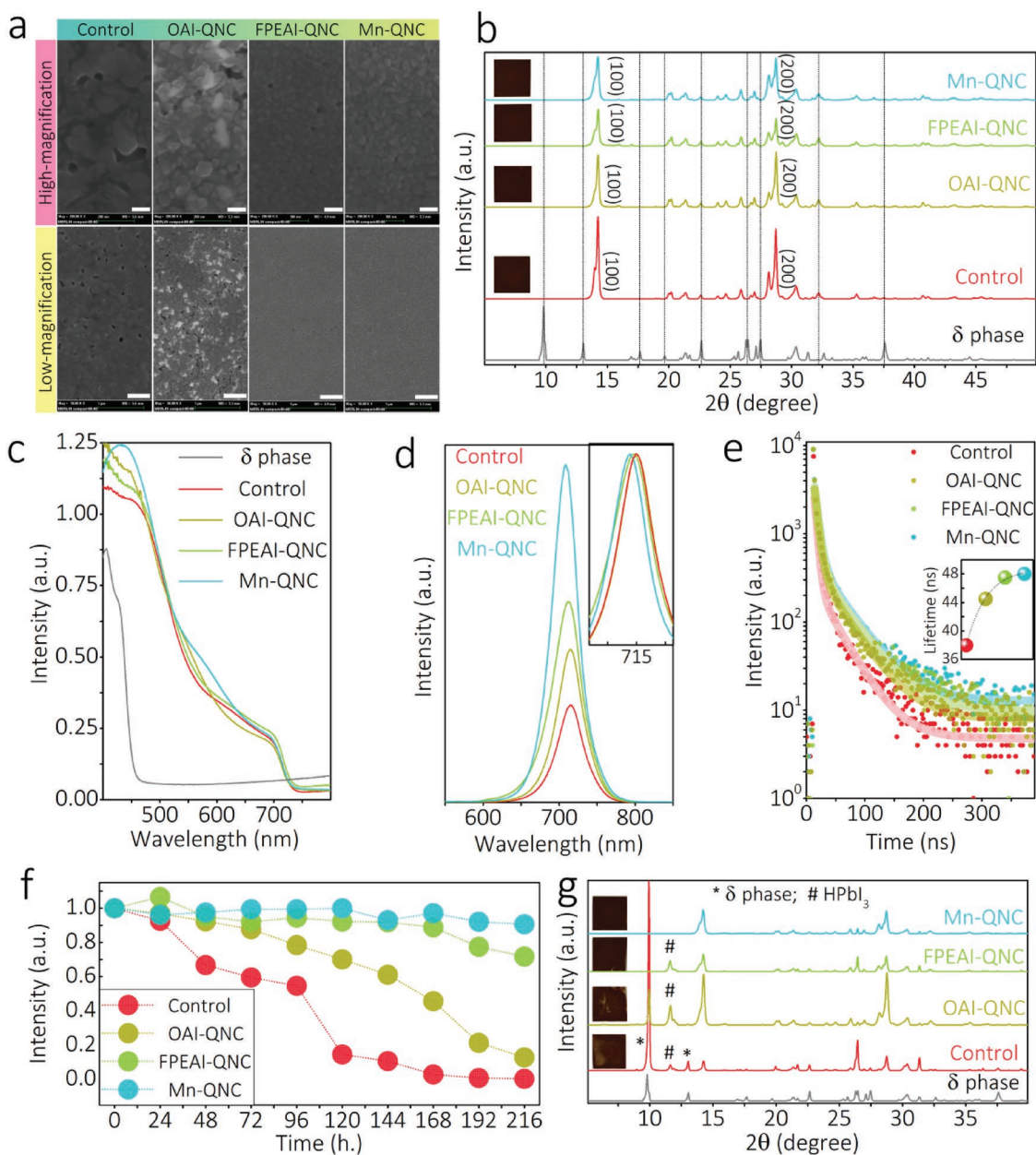


**Figure 3.** a) SEM images of controlled, OAI-based, FPEAI-based, and FPEAI-Mn co-based CsPbI<sub>3</sub> films, scale bar: 100 nm in high magnification and 500 nm in low magnification, respectively. b) XRD patterns, c) UV-vis absorption, d) PL, and e) TRPL of typical corresponding films. f) Stability evaluation in ambient air based on PL in 10 days and g) XRD patterns at 10 days of corresponding films (\* and # belong to  $\delta$  phase and PbI<sub>2</sub>, respectively).

We attempted to fabricate highly efficient p-i-n solar cells by employing the best qualified CsPbI<sub>3</sub> QNC films. Here, the device adopts a structure of ITO (160 nm)/PTAA (6–8 nm)/CsPbI<sub>3</sub> QNC film ( $\approx$ 400 nm)/C<sub>60</sub> (20 nm)/BCP (bathocuproine) (6 nm)/Cu (80 nm). The energy level layout of the whole device is shown in **Figure 4a**. Particularly, the positions of conduction band (CB) and valence band (VB) of  $\alpha$ -CsPbI<sub>3</sub> are estimated to be  $-4.17$  and  $-5.9$  eV from the ultraviolet photoelectron spectra (UPS), respectively (Figure S20, Supporting Information). In parallel, CB and VB positions of yellow  $\delta$ -CsPbI<sub>3</sub> film are  $-3.61$  and  $-6.43$  eV, respectively (Figure S20, Supporting Information), suggesting that  $\delta$  phase should block electron transfer.

Figure 4b shows a typical FIB (focus ion beam)-assisted cross-sectional SEM image of our p-i-n device, revealing close contact between high-quality CsPbI<sub>3</sub> film and transporting layer. What is more, the elemental mappings of energy dispersive spectra (EDS; Figure S21, Supporting Information) are well matched with the device structure. Since EDS is insensitive to the low content F and Mn, we used XPS to further assess the elements (shown in Figure S22, Supporting Information). Atomic ratios of Cs, Pb, I, F, and Mn are estimated as 18.32%, 18.96%, 58.23%, 4.06%, and 0.43%, respectively, which is close to the chemical compositions in our precursors. In terms of carrier dynamics, steady-state PL and TRPL spectra (Figure S23, Supporting



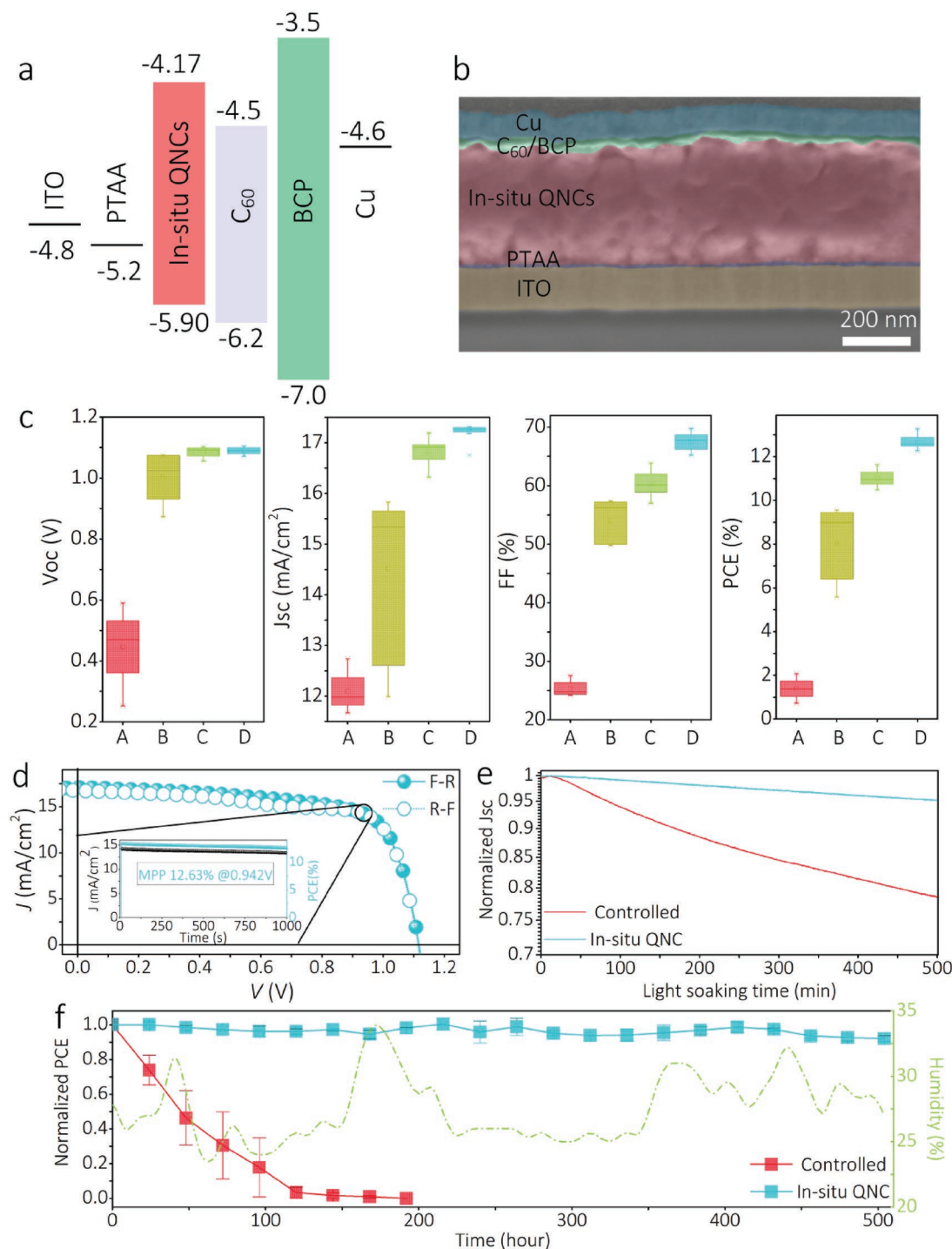


**Figure 4.** a) Energy level layout of used p-i-n device. b) A typical cross-sectional SEM image of in situ assembled CsPbI<sub>3</sub> QNC device. c) Statistical distributions of device photovoltaic parameters using different films, A: controlled, B: OAI-based, C: FPEAI-based, D: FPEAI-Mn co-based. d) J-V curve of the optimal device, where inset shows stabilized power output on maximum power point tracking. e) Normalized  $J_{sc}$  dependent on light soaking time of controlled and in situ QNC device stored in glovebox. f) Normalized PCE dependent on time of unencapsulated controlled and in situ QNC device stored in ambient air.

Information) emphasize efficient holes and electrons extraction from CsPbI<sub>3</sub> QNC film to both transporting layers.

Figure 4c summarizes the statistical distributions of device photovoltaic parameters based on different CsPbI<sub>3</sub> films.

Here, A is without any ligands, B is with OAI ligands, C is with FPEAI ligands, and D is with co-addition of FPEAI and Mn<sup>2+</sup>. The detailed parameters can be found in Table 1. We made our conclusion as follows: 1) Device A shows the worst

**Table 1.** Statistical photovoltaic parameters using different films, A: controlled, B: OAI-based, C: FPEAI-based, D: FPEAI-Mn co-based and the best of D.

Device		$J_{sc}$ [mA cm <sup>-2</sup> ]	$V_{oc}$ [V]	FF [%]	PCE [%]
A		12.09 ± 0.45	0.44 ± 0.14	25.44 ± 1.52	1.39 ± 0.55
B		14.52 ± 1.56	1.00 ± 0.07	54.05 ± 3.52	7.98 ± 1.71
C		16.82 ± 0.27	1.08 ± 0.02	60.34 ± 2.23	11.01 ± 0.38
D		17.21 ± 0.16	1.09 ± 0.01	67.48 ± 1.36	12.65 ± 0.29
Best	F-R	17.10	1.12	70.01	13.40
	R-F	16.78	1.11	71.41	13.33

performance, which is ascribed to the poor film quality and significant exciton nonradiative recombination. 2) In spite of decreased charge coupling, moderate amount of OAI can confine crystal growth and lead to better crystal morphology. The open circuit voltage ( $V_{oc}$ ) of device B increases obviously due to enhanced radiative recombination and carrier lifetime. Nevertheless, a large deviation of the short circuit current density ( $J_{sc}$ ) and the lower fill factor (FF) greatly limit the PCE. This may be attributed to a poor film morphology induced by weaker bonding force between CsPbI<sub>3</sub> and OAI. 3) In device C, all the parameters are improved and become more reproducible, corresponding to its high film quality with enhanced bonding force and conductivity assisted by FPEAI ligands. 4) Compared to device C, device D shows higher  $J_{sc}$ , FF, and almost unchanged  $V_{oc}$ . The best performance should benefit from the highest carrier lifetime of the QNC film with co-addition of FPEAI and Mn<sup>2+</sup> (Figure 3e). Figure 4d demonstrates the highest PCE of 13.40% (forward sweep) and 13.33% (reverse sweep), implying a negligible scan hysteresis of  $J$ - $V$  curve. Additionally,  $J_{sc}$  integrated from the incident photon-to-electron conversion efficiency spectra (Figure S24, Supporting Information) is around 16.7 mA cm<sup>-2</sup>, which is well matched with the value from  $J$ - $V$  curve. Importantly, the PCE of maximum power point tracking under stabilized power output at 0.942 V for 1000 s is around 12.63%, indicating a superb working stability. In addition, similar PCEs under different  $J$ - $V$  scan rates confirm the decent performance (Figure S25, Supporting Information). We also tried to make n-i-p solar cells using the in situ QNC films, and achieved the best PCE of 13.04%, which is comparable to most of the n-i-p based works involving NC films and samples with additives/dopants (Figure S26, Supporting Information). Figure 4e demonstrates device stability under long term (500 min) light soaking in glovebox, where we can observe 21.4% and 4.8% drop of  $J_{sc}$  in the controlled and in situ QNC device, respectively, unveiling reinforced light stability of our in situ QNC film.

We further evaluated the stability of the unencapsulated device in ambient air, as shown in Figure 4f and Figure S27 in the Supporting Information. After storing 500 h in ambient air, in situ QNC device retained 92% of the original efficiency, while the controlled device became almost invalid. This greatly enhanced stability underlines the significance of our rational designed nanostructures. In addition, we measured long-term working stability of the unencapsulated device based on different films by continuous  $J$ - $V$  sweeping under light soaking at 25 °C, 20% relative humidity, as shown in Figure S28 in the

Supporting Information. One can easily find much slower degradation rate of in situ QNC device. This can be explained by enhanced phase stability assisted by the strong bonding force of FPEAI ligands as well as the intrinsic doping of divalent ions. Importantly, this is the first time to track the working stability of unencapsulated CsPbI<sub>3</sub> p-i-n device in ambient air so far. However, the long-term working stability is still unsatisfied. As known to us, there are a lot of complicated reasons, like trapped charge, sensitive interface, and other material instability induced by synergistic effect of water, oxygen, and light.<sup>[7-9]</sup> Consequently, the working stability of CsPbI<sub>3</sub> p-i-n device still has a lot of room to go ahead. In the future, the operational stability is expected to be further improved via interface engineering, material design, and device encapsulation.

### 3. Conclusions

We propose a rational core-shell design of open air low temperature processable CsPbI<sub>3</sub> nanocrystals particularly toward p-i-n solar cells. On one hand, as an alternative shell ligand, FPEAI enhances bonding force with CsPbI<sub>3</sub> lattices and charge coupling between mutual nanocrystals. On the other hand, a new compound H<sub>2</sub>PbI<sub>4</sub> is used to introduce divalent ion Mn<sup>2+</sup> into core lattice, thus suppressing intrinsic traps. Based on this design, stable CsPbI<sub>3</sub> QNC films are readily in situ deposited under low temperature in open air. We achieve the highest PCE of 13.4% for a p-i-n planar structure, which retains 92% after 500 h without encapsulation in ambient air. Importantly, we demonstrate the best performance among the reported works on low temperature processable CsPbI<sub>3</sub> solar cells (Figure S29, Supporting Information). Our work offers a rational design perspective of versatile inorganic perovskite nanocrystals, guiding new possibilities toward robust semiconductor devices.

### 4. Experimental Section

**Material Synthesis**—1) **OAI/FPEAI**: OA and FPEAI (10 mL) were dissolved into 10 mL methanol in flasks in ice baths, and then 20 mL HI (55 wt%) aqueous solutions were added dropwise to the flasks under stirring. After reacting for 30 min, the solutions were dried by rotary evaporator before precipitates appeared. Then the precipitates were washed by anhydrous diethyl ether for four to five times until the precipitates become colorless powders. Finally, all the powders were dried in vacuum oven at 60 °C overnight.

**NMR of FPEAI**: <sup>1</sup>H NMR (500 MHz, D<sub>2</sub>O,  $\delta$ ): 7.39–7.35 (m, 2H), 7.19–7.14 (m, 2H), 3.32 (t,  $J$  = 7.5 Hz, 2H), 3.03 (t,  $J$  = 7.5 Hz, 2H); <sup>13</sup>C NMR (125 MHz, D<sub>2</sub>O,  $\delta$ ): 162.78, 160.85, 132.41, 132.39, 130.78, 130.72, 115.85, 115.67, 40.81, 32.11; <sup>19</sup>F NMR (282.0 MHz, D<sub>2</sub>O,  $\delta$ ): –116.20.

**NMR of OAI**: <sup>1</sup>H NMR (500 MHz, D<sub>2</sub>O,  $\delta$ ): 3.09 (t,  $J$  = 7.5 Hz, 2H), 1.80–1.74 (m, 2H), 1.45–1.31 (m, 10H), 0.91 (t,  $J$  = 7.0 Hz, 3H); <sup>13</sup>C NMR (125 MHz, D<sub>2</sub>O,  $\delta$ ): 39.92, 31.66, 29.05, 28.92, 27.23, 26.36, 22.53, 13.88.

2) **HPbI<sub>3</sub>**: 5 g PbI<sub>2</sub> powders were dissolved into 5 mL dimethylformamide (DMF) in a flask at room temperature, and then 1.9 mL HI (55 wt%) aqueous solutions were added dropwise to the flask under stirring. After reacting for 20 min, the solutions were dried by rotary evaporator before precipitates appeared. Then the precipitates were washed by anhydrous diethyl ether for several times until the precipitates became light yellow. Finally, all the powders were dried in vacuum oven at 60 °C overnight.



3)  $H_2PbI_4$ : The synthesis process of  $H_2PbI_4$  powder was similar to  $HPbI_3$ . The different point was to add 3.8 mL HI (55 wt%) into  $PbI_2$  solutions and other processes were same as that of  $HPbI_3$ . Notice: No further excess recrystallizing and grinding processes were involved for all the powders above.

4)  $H_2PbI_4$  Crystals: High-quality crystals were formed by antisolvent diffusion method: 6.15 g  $H_2PbI_4$  powders were first dissolved into 5 mL DMF, and then the solutions were heated at 100 °C in a toluene atmosphere overnight. During this process, toluene molecules diffused into  $H_2PbI_4$  solutions and reduced its solubility. Afterward, light yellow needle like crystals were formed and collected. Finally, the obtained crystals were dried at 60 °C in an oven overnight.

*In Situ Assembled  $CsPbI_3$  QNC Films*: A series of solutions were prepared by dissolving desired stoichiometric molar ratios of  $0.8 \times 10^{-3}$  M  $HPbI_3$ , CsI, and FPEAI into DMF at room temperature for 2 h with vigorous stirring. With respect to  $Mn^{2+}$  doping, same molar ratio of  $H_2PbI_4$  to  $MnI_2$  was added into former precursors. Before using, all the solutions were filtered by syringe filter with 0.45  $\mu$ m pore size (Whatman). ITO/PTAA substrates were heated at 50 °C for 30 s, before 50  $\mu$ L precursors were spin coated on substrates at 3000 rpm for 40 s. Afterward, the substrates were annealed at 100 °C for 10 min to complete in situ assembled QNC films.

*Device Fabrication*: ITO substrates ( $AMG$ ,  $9.5 \Omega \text{ cm}^{-2}$ ,  $25 \times 25 \text{ mm}^2$ ) were sequentially sonicated in acetone, isopropanol, and deionized water. PTAA solutions (2 mg  $\text{mL}^{-1}$  in toluene) were spin coated on ITO substrates at 6000 rpm for 45 s. Then the substrates were annealed at 100 °C for 10 min.  $CsPbI_3$  QNC films were in situ assembled upon PTAA layer, as described in former part. Then the substrates were transferred into vacuum to evaporate 20 nm  $C60$ , 6 nm BCP, and 80 nm Cu at a rate of  $0.2\text{--}0.3 \text{ \AA s}^{-1}$  to complete the device.

*Material Characterization*: A field emission SEM (AURIGA, Carl Zeiss) was used to investigate the morphologies. The XPS and UPS spectra were obtained using an Axis-Nova (Kratos) spectrometer with a He I (21.22 eV) incident radiation. The TGA measurement was recorded by TG Instruments, USA in  $N_2$  atmosphere. FIB-assisted cross-sectional SEM was obtained by Helios 650 (FEI, USA), where the EDS spectra were acquired at a dwell time of 100  $\mu$ s and 5 eV per channel with a 20 kV accelerating voltage. XRD measurements were performed with an X-ray diffractometer (New D8 Advance, Bruker) with  $Cu K\alpha$  radiation and the XRD patterns were refined by Jade 7.0. The absorption spectra were acquired using a UV-visible spectrophotometer (Cary 5000, Agilent technologies). The PL and TRPL spectra were measured by Fluoromax-4 (HORIBA) instrument.

*Device Characterization*:  $J$ – $V$  curves were measured by a source meter (Keithley 2400, Tektronix) under  $100 \text{ mW cm}^{-2}$ , AM 1.5G simulated one sun using a solar simulator (Sol 3A Class AAA 64023A, Oriel) under calibration using the KG-5 standard Si-cell (91150-KG5, Newport). Step voltage and delay time for the forward and reverse scan were set to 20 mV and 200 ms, respectively. The active area of a device was  $7.29 \text{ mm}^2$  covered with a metal mask. External quantum efficiency (EQE) was measured by a designed EQE system with 75W Xenon lamp (USHIO, Japan).

## Supporting Information

Supporting Information is available from the Wiley Online Library or from the author.

## Acknowledgements

This work was supported by the Global Frontier R&D Program of the Center for Multiscale Energy System (2012M3A6A7054855).

## Conflict of Interest

The authors declare no conflict of interest.

## Keywords

core-shell design,  $CsPbI_3$  quasi-nanocrystals, in situ process, low temperature, p-i-n solar cells

Received: June 4, 2019  
Published online: July 8, 2019

- [1] NREL Chart of Best Research-Cell Efficiencies, <https://www.nrel.gov/pv/cell-efficiency.html> (accessed: June 2019).
- [2] N. J. Jeon, H. Na, E. H. Jung, T.-Y. Yang, Y. G. Lee, G. Kim, H.-W. Shin, S. I. Seok, J. Lee, J. Seo, *Nat. Energy* **2018**, 3, 682.
- [3] M. Abdi-Jalebi, Z. Andaji-Garmaroudi, S. Cacovich, C. Stavarakas, B. Philippe, J. M. Richter, M. Alsari, E. P. Booker, E. M. Hutter, A. J. Pearson, S. Lilliu, T. J. Savenije, H. Rensmo, G. Divitini, C. Ducati, R. H. Friend, S. D. Stranks, *Nature* **2018**, 555, 497.
- [4] H. Tsai, W. Nie, J.-C. Blancon, C. C. Stoumpos, R. Asadpour, B. Harutyunyan, A. J. Neukirch, R. Verduzco, J. J. Crochet, S. Tretiak, L. Pedesseeau, J. Even, M. A. Alam, G. Gupta, J. Lou, P. M. Ajayan, M. J. Bedzyk, M. G. Kanatzidis, A. D. Mohite, *Nature* **2016**, 536, 312.
- [5] H. Cho, S.-H. Jeong, M.-H. Park, Y.-H. Kim, C. Wolf, C.-L. Lee, J. H. Heo, A. Sadhanala, N. Myoung, S. Yoo, S. H. Im, R. H. Friend, T.-W. Lee, *Science* **2015**, 350, 1222.
- [6] K. Domanski, E. A. Alharbi, A. Hagfeldt, M. Grätzel, W. Tress, *Nat. Energy* **2018**, 3, 61.
- [7] N. Ahn, K. Kwak, M. S. Jang, H. Yoon, B. Y. Lee, J.-K. Lee, P. V. Pikhitsa, J. Byun, M. Choi, *Nat. Commun.* **2016**, 7, 13422.
- [8] N. Aristidou, I. Sanchez-Molina, T. Chotchuanachuchaval, M. Brown, L. Martinez, T. Rath, S. A. Haque, *Angew. Chem., Int. Ed.* **2015**, 54, 8208.
- [9] J. S. Manser, M. I. Saidaminov, J. A. Christians, O. M. Bakr, P. V. Kamat, *Acc. Chem. Res.* **2016**, 49, 330.
- [10] W. Li, Z. Wang, F. Deschler, S. Gao, R. H. Friend, A. K. Cheetham, *Nat. Rev. Mater.* **2017**, 2, 16099.
- [11] Q. A. Akkerman, G. Rainò, M. V. Kovalenko, L. Manna, *Nat. Mater.* **2018**, 17, 394.
- [12] G. E. Eperon, G. M. Paternò, R. J. Sutton, A. Zampetti, A. A. Haghighirad, F. Cacialibbi, H. J. Snaith, *J. Mater. Chem. A* **2015**, 3, 19688.
- [13] A. Marronnier, G. Roma, S. Boyer-Richard, L. Pedesseeau, J.-M. Jancu, Y. Bonnassieux, C. Katan, C. C. Stoumpos, M. G. Kanatzidis, J. Even, *ACS Nano* **2018**, 12, 3477.
- [14] G. E. Eperon, M. T. Hörantner, H. J. Snaith, *Nat. Rev. Chem.* **2017**, 1, 0095.
- [15] J. Xi, Z. Wu, B. Jiao, H. Dong, C. Ran, C. Piao, T. Lei, T. B. Song, W. Ke, T. Yokoyama, X. Hou, M. G. Kanatzidis, *Adv. Mater.* **2017**, 29, 1606964.
- [16] F. D. Giacomo, A. Fakharuddin, R. Jose, T. M. Brown, *Energy Environ. Sci.* **2016**, 9, 3007.
- [17] J. Xi, K. Xi, A. Sadhanala, K. H. L. Zhang, G. Li, H. Dong, T. Lei, F. Yuan, C. Ran, B. Jiao, P. R. Coxon, C. J. Harris, X. Hou, R. V. Kumar, Z. Wu, *Nano Energy* **2019**, 56, 741.
- [18] B. Li, Y. Zhang, L. Fu, T. Yu, S. Zhou, L. Zhang, L. Yin, *Nat. Commun.* **2018**, 9, 1076.
- [19] Q. Wang, X. Zheng, Y. Deng, J. Zhao, Z. Chen, J. Huang, *Joule* **2017**, 1, 371.
- [20] T. Zhang, M. I. Dar, G. Li, F. Xu, N. Guo, M. Grätzel, Y. Zhao, *Sci. Adv.* **2017**, 3, e1700841.
- [21] Q. Wang, Z. Jin, D. Chen, D. Bai, H. Bian, J. Sun, G. Zhu, G. Wang, S. Liu, *Adv. Energy Mater.* **2018**, 8, 1800007.
- [22] K. Wang, Z. Jin, L. Liang, H. Bian, D. Bai, H. Wang, J. Zhang, Q. Wang, S. Liu, *Nat. Commun.* **2018**, 9, 4544.

- [23] Y. Hu, F. Bai, X. Liu, Q. Ji, X. Miao, T. Qiu, S. Zhang, *ACS Energy Lett.* **2017**, 2, 2219.
- [24] P. Wang, X. Zhang, Y. Zhou, Q. Jiang, Q. Ye, Z. Chu, X. Li, X. Yang, Z. Yin, J. You, *Nat. Commun.* **2018**, 9, 2225.
- [25] A. Swarnkar, A. R. Marshall, E. M. Sanehira, B. D. Chernomordik, D. T. Moore, J. A. Christians, T. Chakrabarti, J. M. Luther, *Science* **2016**, 354, 92.
- [26] E. M. Sanehira, A. R. Marshall, J. A. Christians, S. P. Harvey, P. N. Ciesielski, L. M. Wheeler, P. Schulz, L. Y. Lin, M. C. Beard, J. M. Luther, *Sci. Adv.* **2017**, 3, eaao4204.
- [27] L. M. Wheeler, E. M. Sanehira, A. R. Marshall, P. Schulz, M. Suri, N. C. Anderson, J. A. Christians, D. Nordlund, D. Sokaras, T. Kroll, S. P. Harvey, J. J. Berry, L. Y. Lin, J. M. Luther, *J. Am. Chem. Soc.* **2018**, 140, 10504.
- [28] H. Bian, D. Bai, Z. Jin, K. Wang, L. Liang, H. Wang, J. Zhang, Q. Wang, S. Liu, *Joule* **2018**, 2, 1500.
- [29] Y. Wang, T. Zhang, M. Kan, Y. Zhao, *J. Am. Chem. Soc.* **2018**, 140, 12345.
- [30] Q. A. Akkerman, D. Meggiolaro, Z. Dang, F. D. Angelis, L. Manna, *ACS Energy Lett.* **2017**, 2, 2183.
- [31] W. van der Stam, J. J. Geuchies, T. Altantzis, K. H. W. van den Bos, J. D. Meeldijk, S. V. Aert, S. Bals, D. Vanmaekelbergh, C. de Mello Donega, *J. Am. Chem. Soc.* **2017**, 139, 4087.
- [32] S. Zou, Y. Liu, J. Li, C. Liu, R. Feng, F. Jiang, Y. Li, J. Song, H. Zeng, M. Hong, X. Chen, *J. Am. Chem. Soc.* **2017**, 139, 11443.
- [33] J. Pan, Y. Shang, J. Yin, M. D. Bastiani, W. Peng, I. Dursun, L. Sinatra, A. M. El-Zohry, M. N. Hedhili, A.-H. Emwas, O. F. Mohammed, Z. Ning, O. M. Bakr, *J. Am. Chem. Soc.* **2018**, 140, 562.
- [34] F. Liu, Y. Zhang, C. Ding, S. Kobayashi, T. Izuishi, N. Nakazawa, T. Toyoda, T. Ohta, S. Hayase, T. Minemoto, K. Yoshino, S. Dai, Q. Shen, *ACS Nano* **2017**, 11, 10373.
- [35] C. R. Kagan, C. B. Murray, *Nat. Nanotechnol.* **2015**, 10, 1013.
- [36] F. Wang, H. Yu, H. Xu, N. Zhao, *Adv. Funct. Mater.* **2015**, 25, 1120.
- [37] M. Long, T. Zhang, Y. Chai, C.-F. Ng, T. C. W. Mak, J. Xu, K. Yan, *Nat. Commun.* **2016**, 7, 13503.
- [38] W. S. Yang, J. H. Noh, N. J. Jeon, Y. C. Kim, S. Ryu, J. Seo, S. I. Seok, *Science* **2015**, 348, 1234.
- [39] B. Zhao, S.-F. Jin, S. Huang, N. Liu, J.-Y. Ma, D.-J. Xue, Q. Han, J. Ding, Q.-Q. Ge, Y. Feng, J.-S. Hu, *J. Am. Chem. Soc.* **2018**, 140, 11716.
- [40] W. Ke, I. Spanopoulos, C. C. Stoumpos, M. G. Kanatzidis, *Nat. Commun.* **2018**, 9, 4785.
- [41] Q. A. Akkerman, M. Gandini, F. D. Stasio, P. Rastogi, F. Palazon, G. Bertoni, J. M. Ball, M. Prato, A. Petrozza, L. Manna, *Nat. Energy* **2017**, 2, 16194.
- [42] L. Protesescu, S. Yakunin, M. I. Bodnarchuk, F. Krieg, R. Caputo, C. H. Hendon, R. X. Yang, A. Walsh, M. V. Kovalenko, *Nano Lett.* **2015**, 15, 3692.
- [43] D. B. Straus, C. R. Kagan, *J. Phys. Chem. Lett.* **2018**, 9, 1434.
- [44] K. Miyata, T. L. Atallah, X.-Y. Zhu, *Sci. Adv.* **2017**, 3, e1701469.